EUROPEAN SOUTHERN OBSERVATORY

Organisation Européenne pour des Recherches Astronomiques dans l'Hémisphère Austral
Europäische Organisation für astronomische Forschung in der südlichen Hemisphäre

VLT PROGRAMME

VERY LARGE TELESCOPE

MACAO for VLTI

System Design Analysis

Doc. No.: VLT-TRE-ESO-15600-2067

Issue: 2.1

Date: 02.02.01

Prepared: J. Farinato, E. Fedrigo, S. Tordo, E. Marchetti, M. Kasper

Name	Date	Signature
	02.02.01	

Approved: R. Arsenault

Name	Date	Signature
R. Arsenault	02.02.01	

Released: N. Hubin

Name	Date	Signature
N. Hubin	02.02.01	

CHANGE RECORD

ISSUE	DATE	SECTION/PARA. AFFECTED	REASON/INITIATION DOCUMENTS/REMARKS
1.0	10.03.2000	All	first issue
2.0	27.09.2000	All	Revised for PDR
2.1	25.01.2001	Sec. 6.2 on power dissipation added	Answer to a PDR comment
2.1	28.01.2001	Sec. 6.3 on possible interference between DM and TTM added	Answer to a PDR comment
2.1	04.02.2001	Sec. 6.4 on DM dynamics added	Answer to a PDR comment
2.1	04.02.2001	Sec. 7.1.1 on Wind Shake changed	Answer to a PDR comment
2.1	04.02.2001	Sec. 7.2 on Piston Analysis updated	To take into account the vibrations introduced by the MACAO system
2.1	08.03.2001	Sec. 7.3 on MACAO CWFS FoV added	Answer to a PDR comment
2.1	10.03.2001	Sec. 7.4 on Tip-Tilt residual added	To justify a spec in the Top Level Requirements
2.1	13.03.2001	Sec. 8 on error budget updated	FDR update

Table of Contents

1 ACRONYMS

AD	Applicable Document
AIT	Assembly, Integration and Tests
AO	Adaptive Optics
APD	Avalanche Photo Diode
BOB	Broker Of Observation Blocks
CWFS	Curvature Wavefront Sensor
CPS	Counts Per Second
DM	Deformable Mirror
ESO	European Southern Observatory
FOV	Field of View
HO	High Order
HW	Hardware
ICD	Interface Control Document
IR	Infrared (1.0-2.2μm)
LOS	Line of Sight, the seeing in the direction that the scope is looking
MACAO	Multiple Applications Curvature Adaptive Optics
Mas	Milli arcsec on the sky
ND	Neutral Density filter
NGS	Natural Guide Star (a point source < 0.2” in size)
OB	Observation Block
OS	Observing Software
OSS	Observing Support Software
PSF	Point Spread Function
RD	Reference Document
SOS	Super OS
STRAP	System for Tip-tilt Removal with Avalanche Photodiodes
SW	Software
TBC	To Be Confirmed
TBD	To be determined
UT	Unit Telescope (8.2-m diameter)
VLT	Very Large Telescope
VLTI	VLT Interferometer (1 – 13 μm)
WFS	WaveFront Sensor
WRT	with respect to

2 SCOPE

The purpose of this document is to present the results of the MACAO for VLTI Adaptive Optics [AO] system simulations, to justify that the functional requirements in RD1 will be met with MACAO-VLTI.

3 APPLICABLE DOCUMENTS

AD 1	*Top-Level Requirements for MACAO-VLTI*	VLT-SPE-ESO-15600-2082	Issue 1.2	01-09-00
AD 2	*MACAO VLTI Technical Specifications*	VLT-SPE-ESO-15600-2245	Issue 1.1	09-03-00
AD 3	*MACAO –VLTI Interface Control Document*	VLT-ICD-ESO-15600-2057(previously issued as VLT-ICD-ESO-11640-2057)	Issue 2.0	05-02-01
AD 4	*MACAO-VLTI Management Plan*	VLT-PLA-ESO-15600-1742	Issue 1.2	12-02-01
AD 5	*MACAO-VLTI List of Deliverables*	VLT-LIS-ESO-15600-2246	Issue 1.1	09-02-01

4 REFERENCE DOCUMENTS

RD 1	MACAO-VLTI System Overview	VLT-TRE-ESO-15600-2251	Issue 1.2	15-02-01
RD 2	Technical Specification for the MACAO WFS Lenslet Array Unit	VLT-SPE-ESO-11640-2146	Issue 2.1	02-02-01
RD 3	MACAO Technical Specifications and Statement of Work for the Two Micro Lenslet Arrays	VLT-SPE-ESO-11640-2460	Issue 1.0	02-02-01
RD 4	Macao VLTI Electronics APD	VLT-TRE-ESO-15600-2269	Issue 2.0	06-03-01
RD 5	MACAO-VLTI Deformable Mirror Design Report	CILAS		28.02.01
RD 6	Effect of DM Dynamics on MACAO Performance	VLT-TRE-ESO-11640-2429	Issue 1.0	31-12-00
RD 7	Technical Specification ESO Adaptive Optics System Deformable Mirror Control	VLT-SPE-ESO-11640-1943	v2.3	14.11.00

5 SYSTEM ANALYSIS

5.1 DESIGN PARAMETERS

All the work presented in this document is based on certain assumptions, concerning the components of the MACAO system that we have simulated and concerning the general observing conditions.
In the following we list these assumptions and the leading reasons for their choice.

5.1.1 Atmosphere

We choose to have a model of the atmosphere with three main layers, matching what is agreed to be the standard average atmosphere in Paranal. The three layers are chosen to match a seeing condition of 0.65" at 500nm, τ_0~4ms, wind speed~11m/s and r_0~16cm, and they are characterised by the following parameters:

Layer	Wind speed	Direction	Weight
Upper Layer (10000m)	33m/s	Horizontal	0.2
Medium Layer (1000m)	5.7m/s	Vertical	0.6
Low Layer (10m)	5.7m/s	Horizontal	0.2

Table 5-1: characteristics of the three layers

We have also tested one case of worse conditions, characterised by a seeing of 1" at 500nm, τ_0~3ms and r_0~10cm.

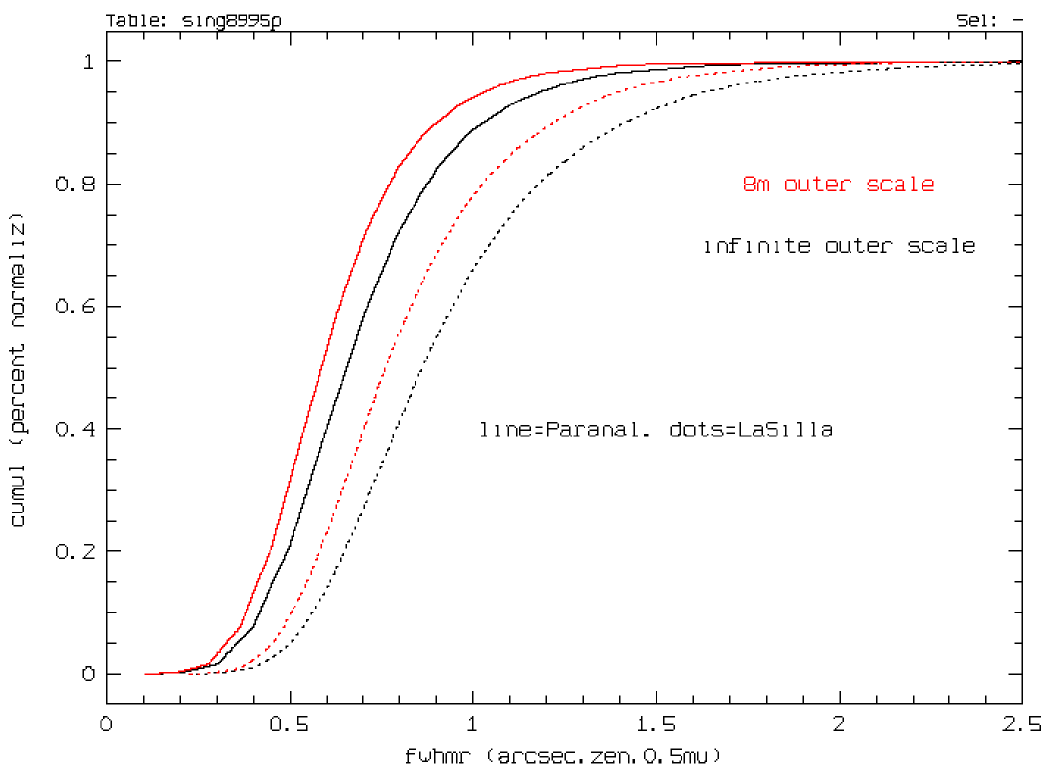

Figure 5-1: Statistical distribution of seeing at Paranal (and La Silla) for the years 1989-1995.

Given these design parameters and the statistical measurement of the seeing at the Paranal site shown in Figure 5-1 (at Zenith) we can conclude that MACAO-VLTI will work 90% of the time and, of course, 50% of the time in the average conditions.

5.1.2 Sky background

Two different values (based on measurement made in La Silla and Paranal) for the sky background have been considered:

- m_V=20.7 mag/arcsec^2 (average dark sky)
- m_V=19 mag/arcsec^2 (bright sky)

5.1.3 Wavefront sensor

This document will present a Curvature Wavefront sensor based on commercial APDs, since that this is the choice which is giving the best performances and the lowest possible risks in the magnitude range of interest matching, in term of performance, the requirements described in AD 1.

5.1.3.1 Curvature Wavefront Sensor

The geometry of the Curvature WFS is described in doc. RD 1, while the technical specifications of the sensor itself are described in doc. RD 2 and doc. RD 3. The justification of the pupil choice is described in sec. 6.5 of this document.

5.1.3.2 Flux detected

The reference flux for the simulations is $4 \cdot 10^5$ detected photons/second at magnitude 15th in the overall 8.2m aperture. This flux is computed by integrating the photons detected from the telescope aperture, including the transmission curves concerning the telescope and the quantum efficiency of the APDs; everything has been integrated in the entire range of sensitivity of the diodes. We have considered a peak of sensitivity for the WFS of 700nm corresponding of course to the sensitivity peak of the APDs.

In Figure 5-2 it is plotted the transmission from space to the Coudé Focus, including the atmosphere, the optics (VLTI input, 6 months aged coatings), the M9 dichroic and the telecentricity lens. The dotted line is taken from the specifications in [AD 1].

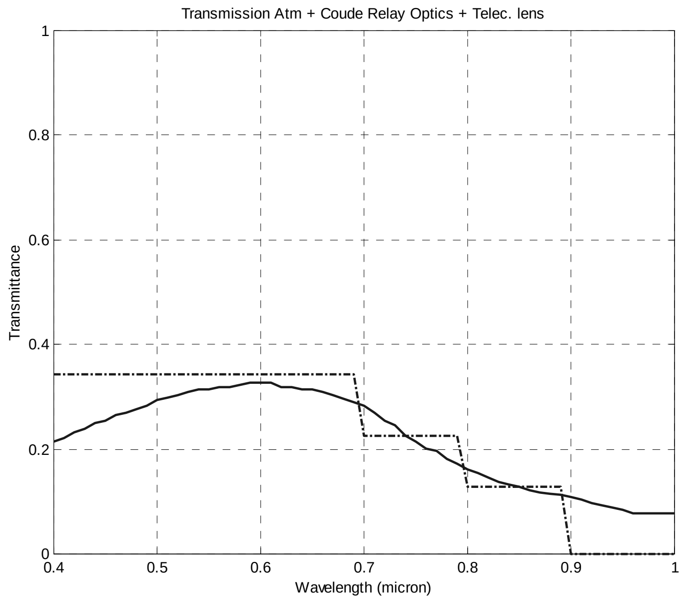

Figure 5-2: light transmission at the Coudé Focus

In Figure 5-3 there is a typical curve (measured in the ESO laboratories) of the APDs' quantum efficiency.

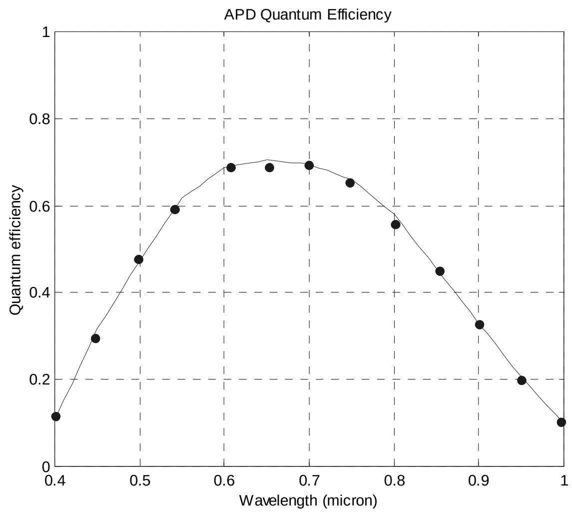

Figure 5-3: measured curves of APDs Quantum Efficiency

The range of photon flux used for the simulation is between 667000cps and 420cps on a single sensor, that correspond to a magnitude range from 9 to 18.
The resulting curves have been scaled to take into account the following additional sources of light losses:

Source	Percentage	Reference
Lenslet array	5%	Literature
Fibers with coupling	10%	Literature
5 WFS mirrors	3% each, average	Internal communication (B. Delabre)
Telecentricity lens	2%	Internal communication (B. Delabre)

The result of these losses is given in Figure 5-4.

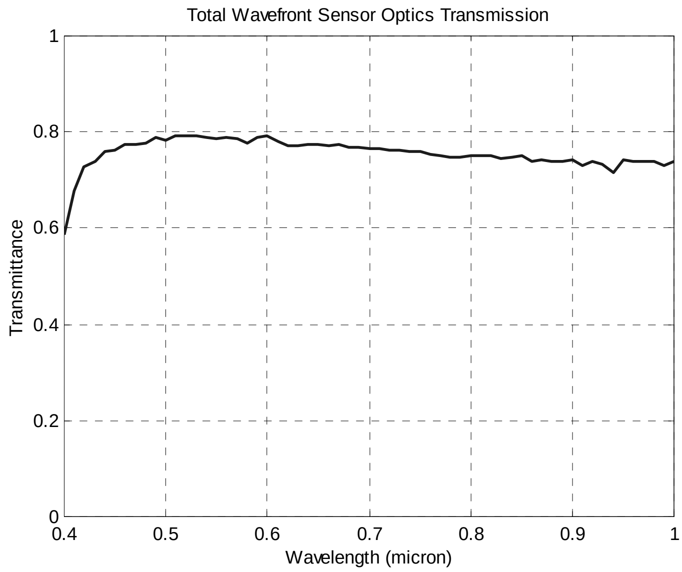

Figure 5-4: Light transmission in the wavefront sensor optics

The cascade of all the three figures gives the final transmittance to the APDs (Figure 5-5).

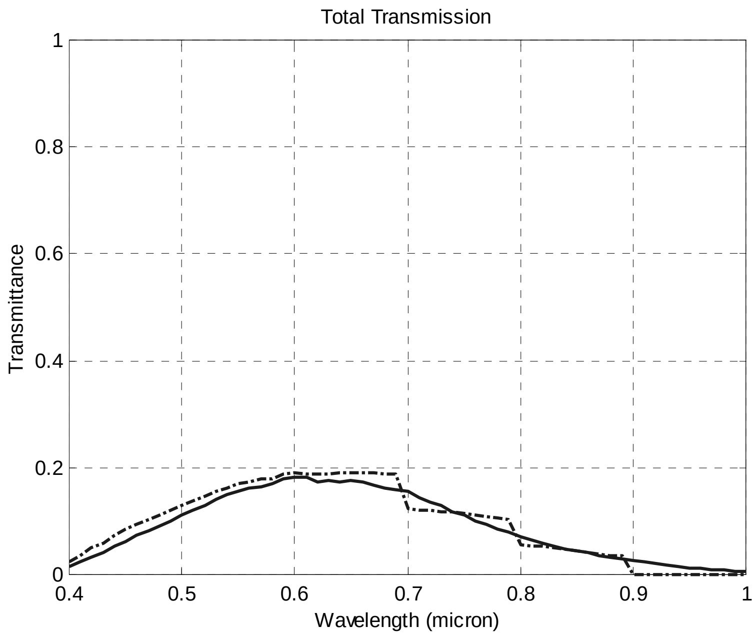

Figure 5-5: Total transmittance to the APDs

5.1.3.3 Detector noise

We choose a value of 250cps for the APDs' dark current, from the Perkin Elmer commercial list (RD 4).

5.1.3.4 Deformable mirror

In the simulation here presented, the mirror is assumed as a bimorph supported in 3 points. Other simulations with a mirror with continuous support showed no difference in Strehl results. The current design for the mirror support is open and left to the final contractor. It is assumed that the change in thickness due to the bending of the mirror is negligible and the dynamic properties of the mirror are not considered since it is a static model (this means that the mirror instantaneously assumes the right shape). Finally, the pupil is assumed to be circular on the bimorph.

5.2 MACAO-VLTI CONTROL LOOP

5.2.1 Structure of the simulation

In order to evaluate the performance of the system, a computer simulation was developed in MatLab. Figure 5-6 shows the structure of the simulation software.

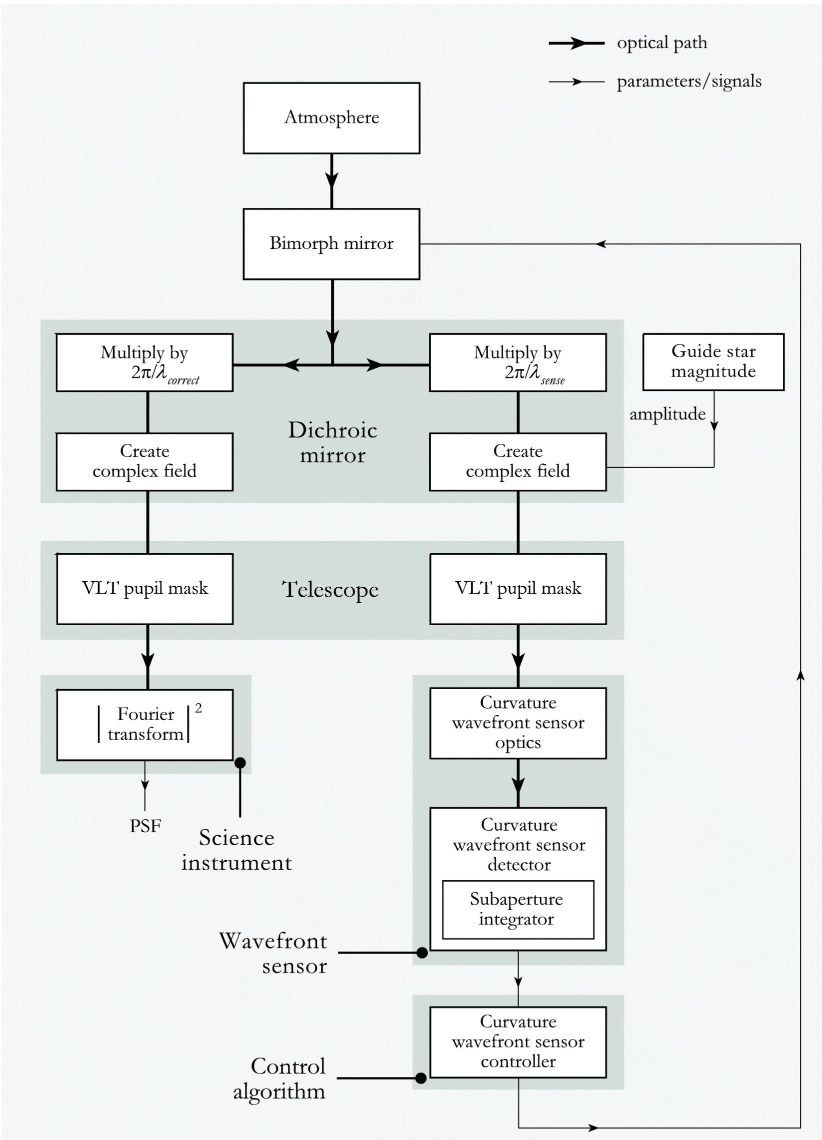

Figure 5-6: Structure of the simulation

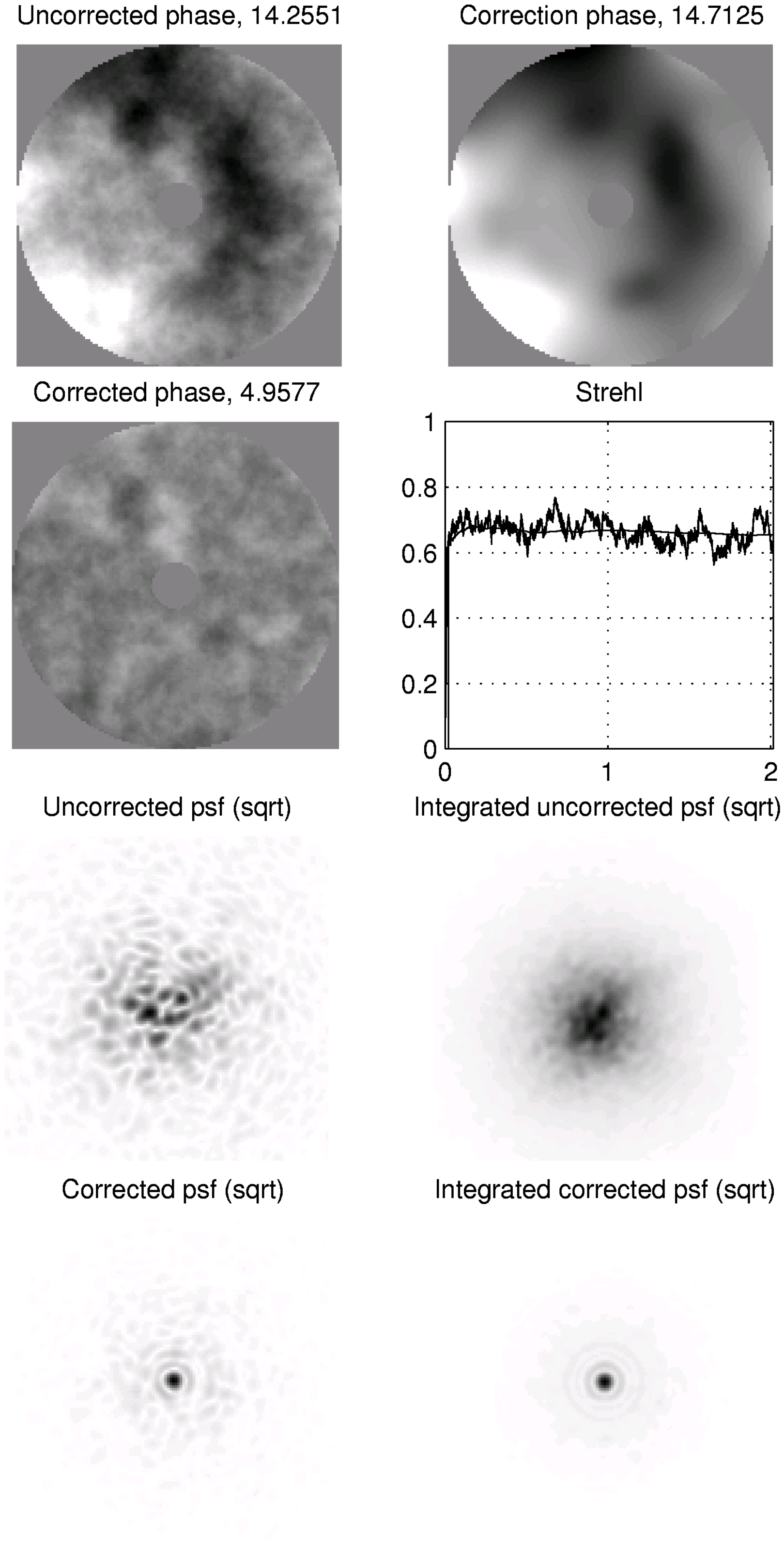

Figure 5-7: The monitoring display, which is updated at regular intervals

To monitor the progress of the simulation, a number of parameters are displayed in a monitoring screen (Figure 5-7), which is updated at regular intervals while the simulation is running. The plots displayed are (from left to right, top to bottom)

- Phase of the uncorrected wavefront.
- Phase correction applied by the bimorph mirror.
- Residual phase aberration of the wavefront.
- Strehl-plot, which contains two curves – the instantaneous and integrated 2.2µm Strehl ratios – as functions of time in seconds.
- Instantaneous uncorrected PSF at 2.2µm.
- Long exposure uncorrected PSF at 2.2µm.
- Instantaneous corrected PSF at 2.2µm.
- Long exposure corrected PSF at 2.2µm.

5.2.2 Parameters used in the simulation

5.2.2.1 General system parameters

Table 5-2 lists general parameters of the system.

Parameter	Value
Membrane mirror frequency	2.1 kHz
Minimum focal length of membrane mirror	0.25 m
Computation delay of controller	0.5 ms

Table 5-2: General system parameters

5.2.2.2 Simplifications of the simulation

Table 5-3 lists simplifications imposed by the simulation.

Parameter	Value
Wavefront sensor wavelength	700nm
Science instrument wavelength	2.2µm
Wavefront sampling distance	6.25cm
Atmosphere update rate	4.2kHz
Temporal sampling rate of membrane motion	33.6kHz
Total simulation time per magnitude	2.0s

Table 5-3: Simplifications imposed by the simulation

5.2.2.3 Loop gains and integration times

Table 5-4 lists the optimised loop gains, integration times and corresponding update frequencies used for guide stars of magnitude 10 to 18 for 0.65" and 1.0" seeing.

Guide star magnitude	0.65" seeing				1.0" seeing			
	Integr. time [ms]	Update freq. [Hz]	Loop gain	Cl. loop freq. [Hz]	Integr. time [ms]	Update freq. [Hz]	Loop gain	Closed loop freq. [Hz]
10	2.86	350	0.6	30	2.86	350	0.7	35
11	2.86	350	0.5	25	2.86	350	0.6	30
12	2.86	350	0.4	20	2.86	350	0.5	25
13	2.86	350	0.3	15	2.86	350	0.4	20
14	4.76	210	0.6	20	4.76	210	0.6	20
15	4.76	210	0.5	14	4.76	210	0.5	14
16	6.67	150	0.3	13	6.67	150	0.3	13
17	14.8	67.7	0.3	6	14.8	67.7	0.3	6
18	40.0	25.0	0.3	5	40.0	25.0	0.3	5

Table 5-4: Optimised loop gains, integration times and update frequencies used in the simulation

5.2.2.4 Simulated conditions

Four simulation runs were made using different seeing conditions, dark current of the detectors, sky background magnitude and field of view. The parameters used for the runs are listed in Table 5-5.

Simulation number	Seeing ["]	Dark current [s^{-1}]	Sky background	Field of view ["]
1	0.65	100	20.5	1.0
2	0.65	250	20.5	1.0
3	0.65	250	19.0	2.0
4	1.0	250	20.5	2.0

Table 5-5: Simulated conditions

5.2.3 Simulation results

Figure 5-8 shows the results of the simulation.
This plot does not include the full error budget, which will be included later in section 8, as a shift on the Y axis (different Strehl ratio delivered).
Not all the sources of loss of light have been taken into account to determine the number of photon counts per subaperture per second. The remaining losses (wavefront sensor optics and telecentricity lens) will be included later in section 8.3 as a shift in Y axis (different apparent magnitude).
Different APD dark currents and sky background magnitudes have been considered: their effect becomes relevant only in the faint star region, where the curve is approaching the natural Strehl ratio, i.e.: the Strehl ratio without correction.

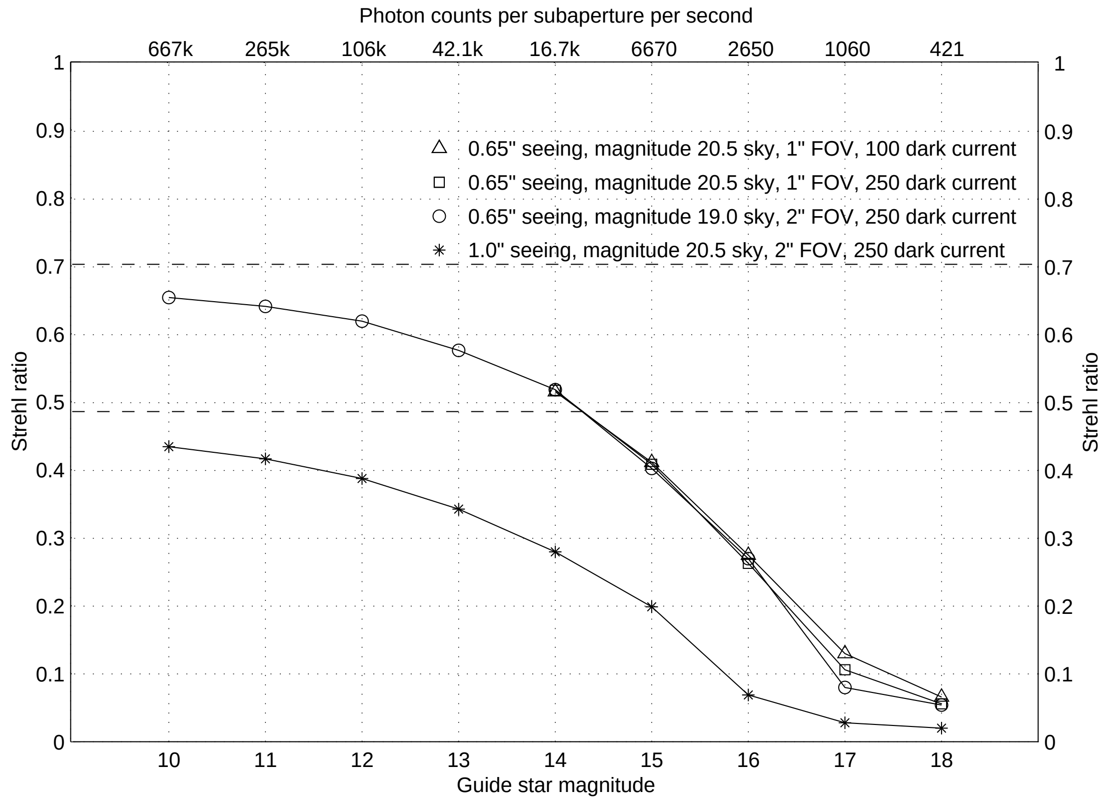

Figure 5-8: Resulting Strehl ratio in K-band (2.2 µm). The dashed horizontal lines indicate the performance of a noise-free system with infinite bandwidth and flux for the two different seeing conditions

6 DESIGN ASPECTS

6.1 NEUTRAL DENSITY WHEEL

In the current design we have 8 positions available for neutral density filters (plus one position for the glass) in the neutral density wheel. Applying the filters we can move the guide star magnitude along the curve in Figure 5-8 and thus we will have a drop in performance if the distance between the filters is too big.
MACAO can run without any filter up to magnitude 9 which correspond, approximately, to 2 million counts per second in each APD, the safety margin.
Simulations show that for magnitude 8 we get a Strehl of 66% and for magnitude 11 we get 64% (mv=10.5 → 65%).
With a spacing in magnitude equals to 1.25 mag, the set of filters allow MACAO-VLTI to operate up to magnitude –1 with a loss in performance approximately equal to 1%.

6.2 POWER DISSIPATION

In RD5 there is a complete analysis (Sec. 6.1) concerning the total power dissipation due to the heat sources present in the wavefront area. The grand total is 18W, and we estimate that a significant part of it will be sunk into the mechanical structure of MACAO and of the XY table. In particular, the design of the XY table is made in a way that maximises the heat conduction between the motors and the frame.
Measurements made in Paranal on motors used in the Coude` platform (very similar to the one that will be used for the XY table) have shown no measurable differences of temperature between the motors themselves and the surrounding air.
If it will turn out to be a problem, the housing of the motors could be insulated (we already check that there is enough space for that between the motors and the housing), but for the time being we do not expect any influence on the system performances.

6.3 DM EFFECT ON THE TTM CAPACITIVE SENSORS

After gathering informations both from the TTM designer (Pierre Gigan – Observatoire de Meudon) and from the company that will provide the Capacitive Sensors (FOGALE), we now have more details concerning the capacitive sensors that will be used for the TTM:

- The sensors are shielded and the shield is connected to the ground, to prevent any possible interference of external electromagnetic fields (the company claims that they are insensitive to electromagnetic fields)
- The shielding is of the tri-axial type: signal, normal shield, plus a supplementary sleeve to the ground (for sensor and cables).
- The pair sensor-target creates a Faraday cage around the electrode.
- The carrier signal is at a frequency of 50 kHz and a synchronous demodulator allows a high rejection of the perturbations.

Given that the DM control voltages will be issued typically with voltage 100 RMS, and at a maximum frequency of 350 Hz, it is clear that they will have low or no impact.
Furthermore, the position of the capacitive sensors on the TTM has been moved in order to maximise the distance between them and the DM actuators and each sensors is in the "shadow" of the TTM actuators, which provide additional shielding.
These sensors have been developed to maintain low noise level in extremely high EMI environment:

- "Micro-machine de force": where the sensor is in close proximity to a magnetic levitation system
- Interferometric Microscope: a 1000 V piezo actuator is controlled by such sensor to an accuracy of 0.1nm

- Used also in particles accelerators: CERN, ESRF, EDF, "Commissariat a L'energie Atomique" CNRS, CNES.

Considering all these information, we do not think that the High Voltages used to drive the DM actuators will interfere at all with the capacitive sensors.

6.4 DM RESONANCE ANALYSIS

All the simulations, on which this report is based, do not take into account the effect of the resonance frequencies of the deformable mirror. According to the design report [RD 5] from CILAS, the DM manufacturer, the central electrode of the 60-element DM will have the following characteristics and transfer function:

Model	Diameter (mm)	Thickness (mm)	f1 (Hz)	Gain (dB) at resonance f1	f2 (Hz)	Gain (dB) at resonance f2
BIM60	150	2.6 (2 PZT and 0.6 glass)	~250	~8	810	~25

Table 6-1: Foreseen DM parameters

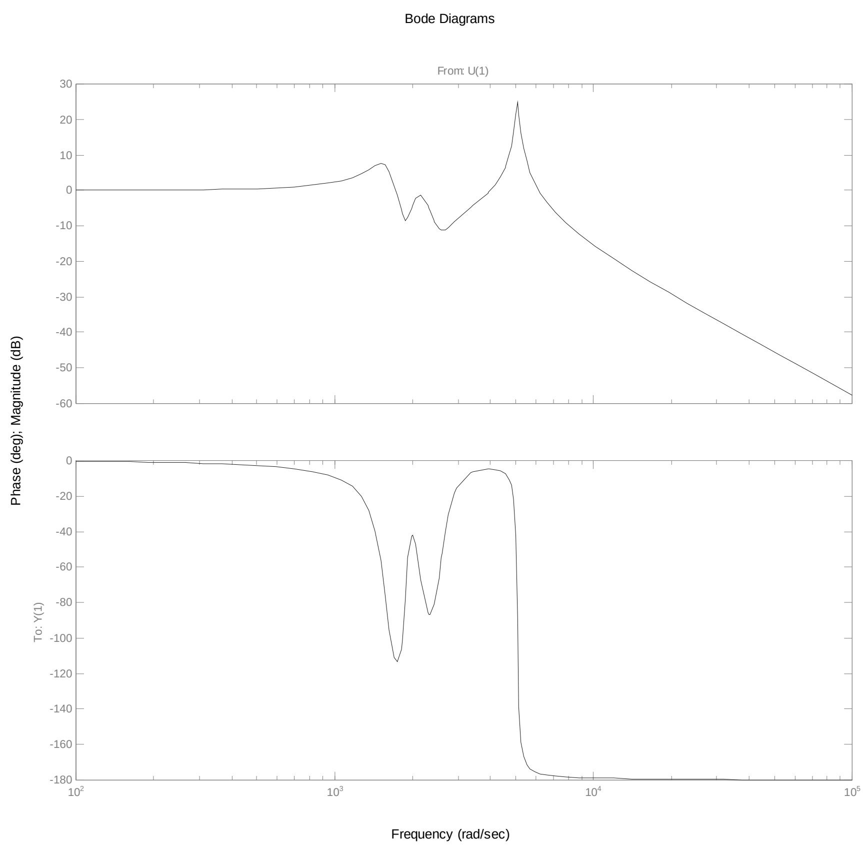

Figure 6-1: Synthetized transfer function

The presence of these resonance frequencies could potentially affect system performance since the DM is deviating from the perfect mirror response which has been assumed in the simulation, i.e.: a mirror which adapt instantly to the required change in shape.
A study [RD 6] has been written to study this problem and hereby we report only the summary and conclusions.

Using table Table 5-1 and extrapolating the transfer function of a similar smaller mirror (bimorph 13 elements) we set up a series of simulations. The DM has been modelled as a bank of filters each sharing the same Transfer Function connected to a perfect mirror simulated through its influence functions.
We analysed the model in terms of mirror dynamics, Strehl loss and piston effect. We also analysed a shaping filter as a way to compensate for this effect.

In the following table we recall the results we found analysing the Strehl degradation due to the resonant mirror modes. We computed the Strehl degradation factor and we computed which is the equivalent phase lag to obtain the same degradation factor. To solve the problem of the degradation in performance one can design a shaping filter, which will act in open-loop simply compensating for the undesired mirror dynamics.
But implementing the shaping filter in the RTC will cause the control loop to run slower. The last column I the table shows what is the computational delay that produces the same error as the resonant modes. If the additional computation required to solve the error given by the effect of the resonant modes is longer that the value in the table, then this phase lag itself will add more error than the error the same algorithm should remove, and thus it is not convenient.

Currently the control loop is designed to complete one cycle in 0.5ms, given the full computer power. The shaping filter implemented in the RTC will take half of the computer power, doubling the time required to complete one cycle. At least for the first three cases in the table, the benefit of the shaping filter will be destroyed by the additional phase lag which is exactly in the same order.

Corrected Strehl With resonant modes	Absolute Degradation	Relative Degradation	Degradation Factor	Equivalent phase lag
65%	1.5%	2.3%	97.7	0.4ms
45%	1.5%	3.3%	96.7	0.5ms
30%	1.5%	5%	95	0.7ms
10%	1.5%	15%	85	1.3ms

Table 6-2: Summary of the simulations described in [RD 6]. The first column gives the Strehl after correction with the resonant modes under certain conditions (see [RD 6], the second the absolute degradation in respect to the case with an ideal mirror (Strehl(ideal)-Strehl(real)), the third the relative degradation which is the Strehl degradation factor given in the fourth column. From this value we compute the corresponding σ^2 and what will be the computing phase lag that will give the same error variance.

This means that if the shaping filter is really necessary, it cannot be implemented in the Real Time Computer. The only reasonable solution is to put this filter into the HVA electronics and the most promising solution seems to be an additional computational module.
But we've also seen that such a filter is very sensitive to a correct tuning (during installation) and to the constancy of the mirror properties potentially leading to worse results in case of bad tuning.

On the second effect, the piston, we discovered that there is no effect at all (it is negligible) so no counter-measures are suggested.

So the conclusion is:

- If a loss of 1.5% of Strehl is acceptable, nothing should be done for the problem of the resonant mirror modes.
- In case this will turn out to be a problem, the proposed solution is an additional computational module to be installed on the HVA LCU which will implement a simple (maximum 4th order IIR filter) shaping filter.

6.5 MACAO-VLTI PUPIL DEFINITION

We have explored different solutions, changing the number of actuators and the geometry of the mirror. Once it was established that the optimal number of actuators was around 60, we have explored 9 different geometries, with 59, 60 and 61 actuators. The subapertures had always-equal area illumination.

Changing the geometry, the fitting error can vary, and the noise propagation on the mirror modes also varies. We have looked at the noise propagation coefficients for tilt and for the total of the mirror modes, as selection parameter.

Running the different geometry in closed loop with the numerical simulation code of F. Rigaut, with a bright star (mv=8), we have verified that the chosen 60 element geometry of MACAO gives the best results in terms of residual variance and Strehl ratio.

In the following we report as an example three of the best cases found. The difference in residual closed loop variance is marginal for the different geometry. There is difference in the noise propagation coefficients, which turns out useful with faint NGS.
All variances are computed at 700nm.

1. Case 1: 60 electrodes, 4 rings (6 12 18 24)
   Variance of noise on tip-tilt: 167.7 rad^2
   Total variance of noise: 216.7
   Bright star, Closed loop corrected variance: 3.00 rad^2

2. Case 2: 60 electrodes, 5 rings (4 8 12 16 20)
   Variance of noise on tip-tilt: 156.8 rad^2
   Total variance of noise: 198.7
   Bright star, Closed loop corrected variance: 2.89 rad^2

3. Case 3: 61 electrodes, 5 rings (1 6 12 18 24)
   Variance of noise on tip-tilt: 163.1 rad^2
   Total variance of noise: 211.6
   Bright star, Closed loop corrected variance: 3.12 rad^2

The closed loop simulation used Kolmogorov turbulence, the VLT pupil and central obstruction were correctly simulated.
The solution adopted for MACAO is the second one.
The chosen geometry for MACAO VLTI, with 5 rings and 4-8-12-16-20 actuators gave the best performance, for the noise propagation and for the closed loop residual variance.

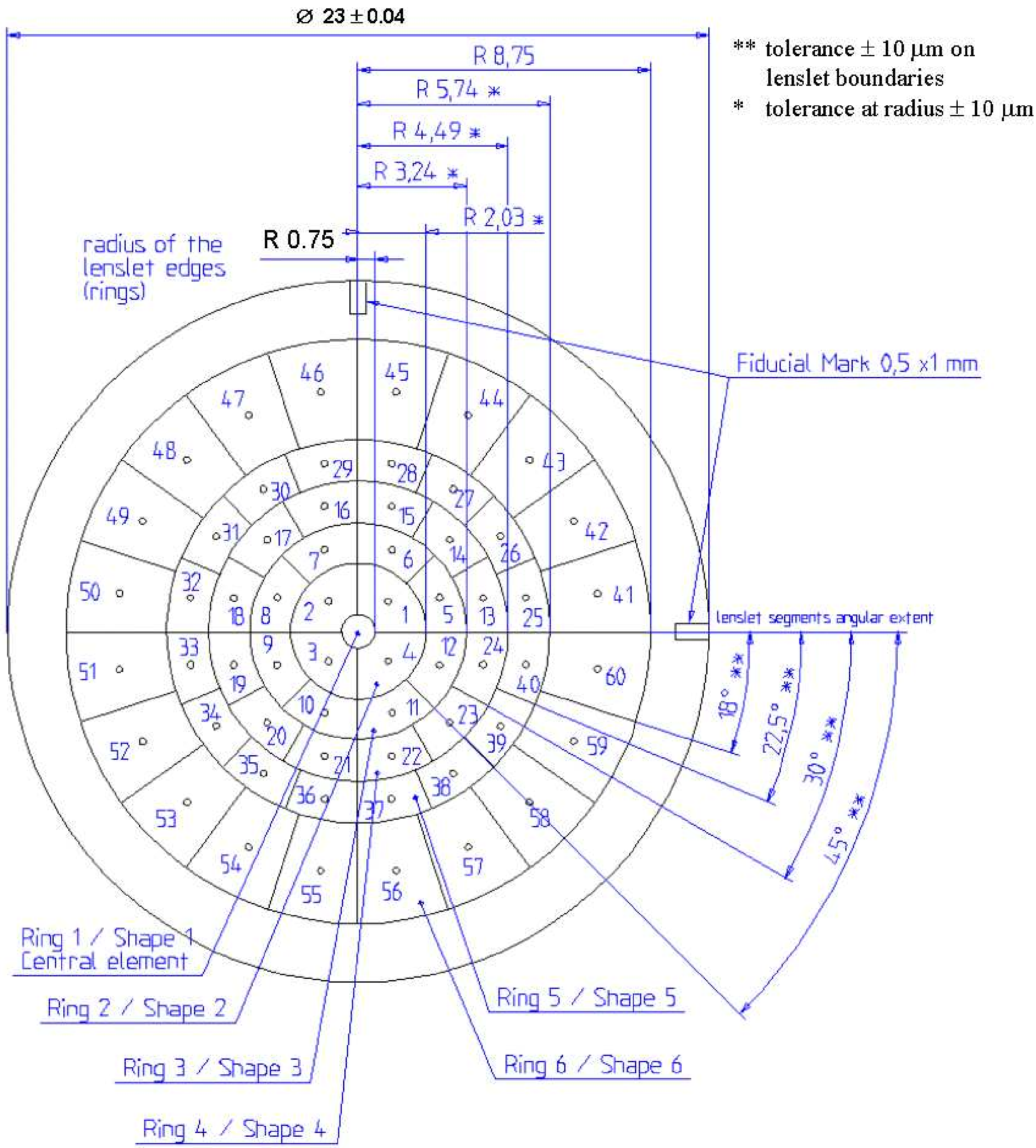

Figure 6-2: MACAO VLTI sensor geometry

6.6 LOOP PERFORMANCE

The control loop can be modeled with the following open loop transfer function (Roddier, 1999):

$$G(s) = \left[\frac{1 - e^{-Ts}}{Ts}\right]^2 e^{-\tau s} C(z = e^{Ts})$$

where C(z) is the transfer function of the real-time computer except its delay, which is taken into account by the term $e^{-\tau s}$. T is the period of control loop. Choosing as a controller a simple integrator with gain control (PI controller):

$$C(z) = \frac{K}{1 - z^{-1}}$$

we have:

$$G(s) = \frac{1 - e^{-Ts}}{(Ts)^2} e^{-\tau s}$$

with:

Parameter	Value	Value	Value
T	2.86 ms	4.76 ms	6.67 ms
τ	0.5 ms	0.5 ms	0.5 ms

Table 6-3: Parameters

In Figure 6-3 we show the Nyquist plot for the stability of the system for T=2.86 ms. The curves are plot for K=0.6, 1.2, 3 and 5. The curve plot in dotted line is relative to K=3, the limit for the stability. For K=1.2 the stability margin, the dotted circle, has radius equal to 0.5.

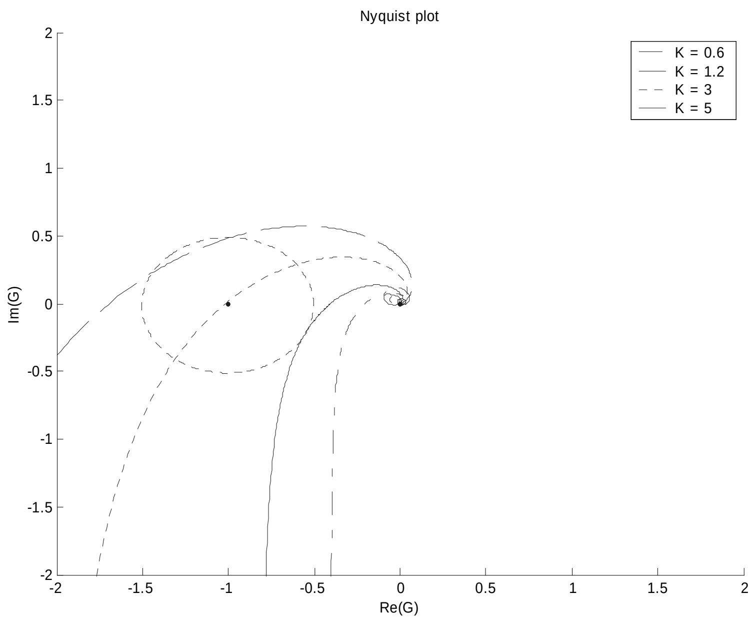

Figure 6-3: Nyquist plot for the open-loop transfer function

We can see better the stability margins in the Bode plot in Figure 6-4 where they are shown with the dotted lines.
Asking for a phase margin of 45 degrees we determine which is the gain that has this margin. The value of this safe limit gain is K=1.2. With this gain we have a gain margin of approximately 8 dB.
In the closed loop plot we can determine the bandwidth of the system for the gains we have chosen.
The closed loop function is determined by:

$$H(s) = \frac{G(s)}{1 + G(s)}$$

For τ=2.86 ms and K=0.9 or K=1.2 the bandwidth at 3dB is approximately 100Hz (Figure 6-5).
The gain at K=1.2 has also an overshoot of 2.6 dB, which is acceptable.

The following Table 6-4 summarizes the results for the three cases we considered.

Integration time (ms)	Stability boundary	Limit gain	-3dB Bandwidth	Overshoot
2.86 ms	K=3.0	K=1.2	125 Hz	2.6 dB
4.76 ms	K=3.6	K=1.3	79 Hz	2.1 dB
6.67 ms	K=3.8	K=1.4	58 Hz	2.2 dB

Table 6-4: Gain vs Integration time

Figure 6-6 shows the error transfer function and Table 6-5 the corresponding system bandwidth using the 0-dB closed-loop frequency.

Integration time (ms)	Stability boundary	Limit gain	0dB Bandwidth	Overshoot
2.86 ms	K=3.0	K=1.2	52 Hz	2.6 dB
4.76 ms	K=3.6	K=1.3	36 Hz	2.1 dB
6.67 ms	K=3.8	K=1.4	27 Hz	2.2 dB

Table 6-5: Gain vs Integration time

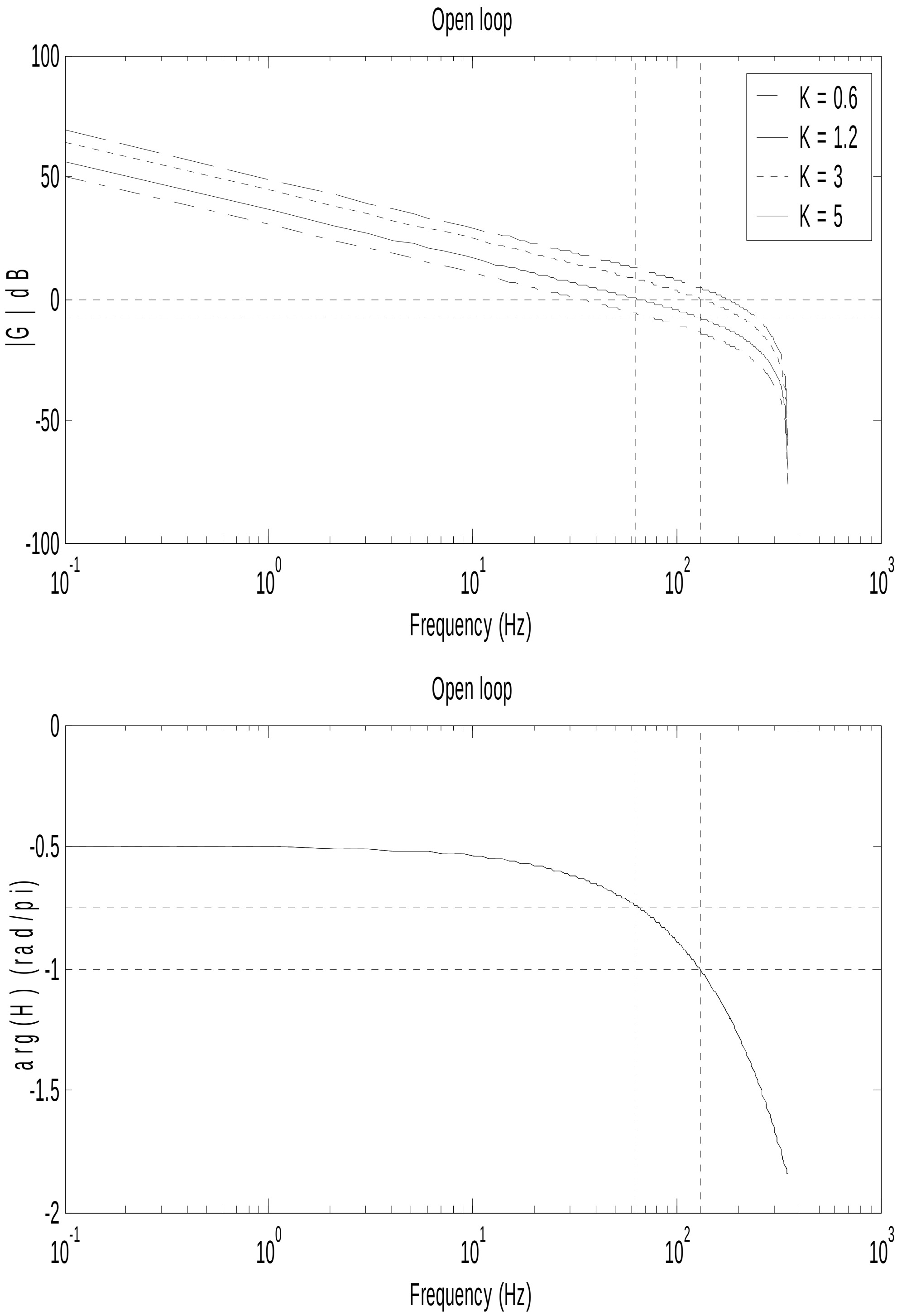

Figure 6-4: Open Loop Bode plot with stability margins

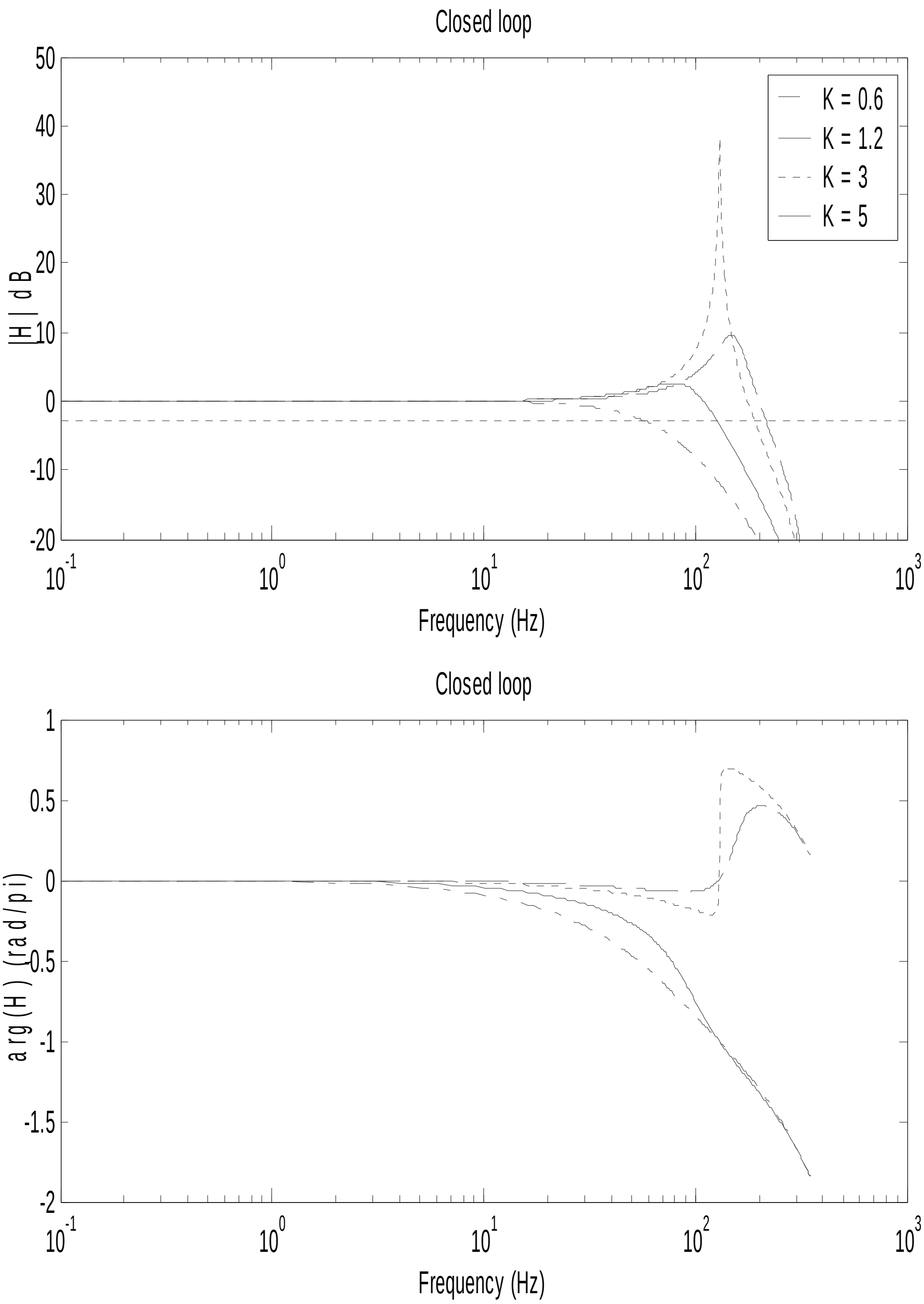

Figure 6-5: Closed loop Bode plot with bandwidth

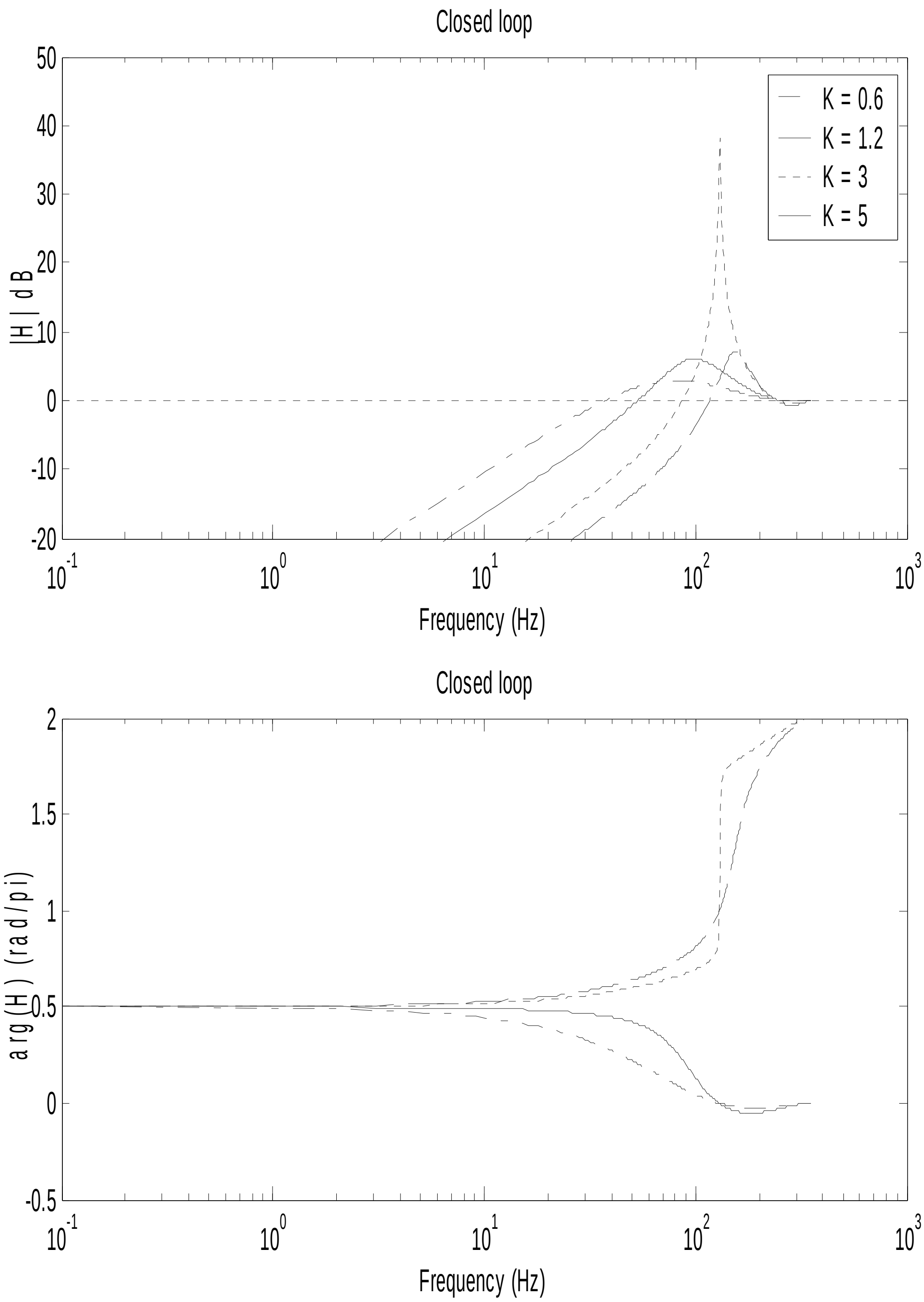

Figure 6-6: Error-rejection transfer function

7 FUNCTIONAL ASPECTS

7.1 CHOPPING

We are requested to chop with a frequency of 1Hz (goal 5Hz) and a duty cycle of 50% (goal 80%).
The averaged exposure time for a scientific image is 10 minutes[1], and so our system is supposed to accomplish chopping for at least this time.
We will make an analysis with the purpose to show that we can meet the requirement of 1Hz.

7.1.1 Wind Shake

No field stabilisation is performed when MACAO is in use and, moreover, while the telescope is chopping with MACAO active. Thus only when the system is looking at the object, the field is stabilised by the AO system, while when the system is looking at the Sky, it is under the effect of the wind-shake. Checking the results which are coming out from the analysis of the rms error on UT2 in x and y axis from the guide camera, the worst case of the oscillation is 0.38” in X axis and 0.18” in Y axis, and the frequency of this oscillation is always below 20Hz. This means that as soon as we will go back to the star, there will be a displacement on its position.
The system has to be tuned to the worst case, but we will present also an averaged situation.
Considering the worst value of 0.38” in X axis and 0.18” in Y axis and summing them in quadrature, we come to a displacement which is roughly 0.42” rms (wind-shake only).
Adding the effect of the atmospheric tip/tilt (in our example we considered 1” seeing and 10 m/s wind speed), this is the displacement we can expect when the system comes back to the star position. If the system is able to close the loop, this action will reset the ‘random variable’ which causes the displacement, so the variance of the displacement if the chopping is working correctly is different from what we have just computed and certainly lower. If the chopping frequency increases, less time is left to this ‘random variable’ to evolve so the variance of the expected displacement will be inverse function of the chopping frequency.
Simulation the AO correction and the wind shake effect we have[2]:

- 0.51 “ RMS for a chopping frequency of 1 Hz
- 0.13” RMS for a chopping frequency of 5 Hz

We assume to use an average value for the membrane stroke which gives a field of view of 2” and we assume that the star is a point source. We also assume that the AO system will be able to bring the star at the centre of the FoV and close the loop even in the limit case when the star is exactly on the boundaries of the FoV but some light still reaches the sensor.
Thus the probability that the star is beyond this limit is 5% (1Hz) and 1% (5Hz), that is the probability not to close the loop immediately after the chop. We then compute the expected time to fail closing the loop in the two cases:

Chopping FRQ	Probability to loose the loop	Mean time to loose the loop
1Hz	5%	20 seconds
5Hz	1%	20 seconds

Obviously, running the loop at 5Hz we can take advantage of the AO correction and lower the probability to loose the loop when returning on the star but running faster means also that the system has more chances to loose that loop so at the end the two cases are equivalent.

[1] Internal communication from VLTI.
[2] Thanks to B. Koeler.

7.1.2 Chopping Frequency

To increase the probability to lock the reference object after the image on the sky, we have to close the loop in two incremental phases:

- In the first phase the AO loop uses only the Tip-Tilt correction on, to re-centre the star in the cwfs FOV.
- Once the tilt loop is closed, we enable also the High Order correction.

Now, the most important thing is to quantify how long the bootstrap lasts for the two different phases. From the simulation, **considering the median seeing of 0.65” and that the star is back after chopping within a circle of 0.7” at** 4σ, the bootstrap phase for the high order loop lasts:

- 10 cycles for a 10th visual magnitude star, with an integration time of 2.9ms
- 24 cycles for a 16th visual magnitude star, with an integration time of 6.7ms

We can reasonably assume that the bootstrap phase for the tilt system lasts for the same number of cycles. These considerations lead to a total bootstrap time of:

- 58ms for a 10th visual magnitude star
- 320ms for a 16th visual magnitude star

Considering that the settling time of M2 is ~20ms, and an idle time of 50%, we can compute the global time needed for a chopping cycle (Fig. 7-1).

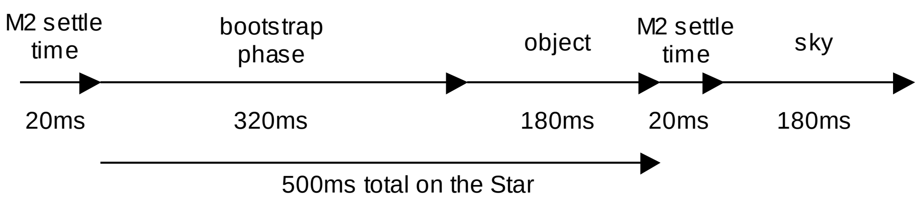

Fig. 7-1: Chopping time on a star of visual magnitude 16th

The total time is 720ms, i.e. a chopping frequency that is slightly more than 1Hz. Scaling to 1Hz means to enlarge the working window of the system to 320ms both for the sky and for the object, which means a duty cycle of 66%:

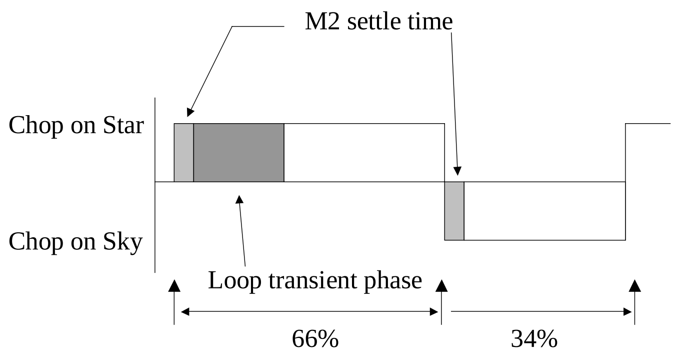

Figure 7-1: Duty cycle definition

7.1.3 Final considerations

It is clear that considering the telescope shacking due to the wind, the result presented in the previous section is the best MACAO-VLTI can do in the worst case of a star of m_V=16.

Considering instead a better situation with a m_V=10 star, the situation is the one described in Fig. 7-2, from

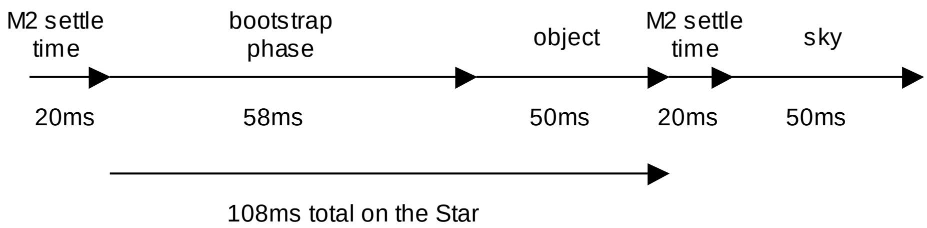

Fig. 7-2: Chopping time on a star of visual magnitude 10th

which it is clear that we can meet also the 5Hz goal with a 50% duty cycle. The situation might be even better if we consider a tracking error of the telescope of 0.7" PTV at 4σ, because in this situation MACAO can perform a 90-minute exposure without failures with a 5Hz chopping rate.

7.2 MACAO-VLTI PISTON ANALYSIS

According to VLTI specifications (AD1) the piston term introduced by MACAO-VLTI must be constrained. We want to report here on the four possible sources of piston fluctuations we have identified.

7.2.1 The imperfect removal of piston mode implemented in the control loop algorithm.

The piston mode removal is implemented in the actual control loop algorithm in a two-steps process.
The first step has the task of keeping the voltage applied to the electrodes within the range. The rational for this is that the system has a mode that is not controllable (in control theory sense), the piston mode, but, due to the noise that affects the process of measuring the interaction matrix, a component of this mode exists.
At each iteration of the closed loop, the piston vector is scaled and then subtracted from the mirror commands removing the piston from the command space. Given the shape of the electrode's influence functions this contribution is only partially removed in the mirror space. The second stage has the task of removing this component deliberately adding a small component of piston in command space. This component is guaranteed not to diverge because of the first step. This algorithm is also described in the MACAO-VLTI RTC software specification document.
This process won't be perfect since it is based on the measurements of the influence functions and on the interaction matrix measurement, which is noisy. Thus we expect a residual piston term.

Using simulations we have computed the amount of piston subtracted in closed loop from the drive commands (see also "effect of DM dynamics on MACAO performances" VLT-TRE-ESO-11640-2429). The error made because of an imperfect removal will therefore be only a fraction of this subtracted piston. The simulation gives a maximum rms (WFE) fluctuation of 400nm over 48ms and 900nm over 290ms to remove (@mv=10 and 0.65" seeing). We computed that to reach the specification performances we must calibrate the piston of each influence function with a maximum of 1% error (standard deviation of the error over the 60 measurements). This guarantees, in the simulated environment, a residual rms piston term of 18 nm over 48ms and 26 nm over 290ms (see also piston error budget table).
Nevertheless, we still need to complete our measurement scheme to verify the exact error made. A work package with an external contractor has been placed to work on this subject both on the measurement and on

the algorithm aspects. On Paranal the best case would be to use the fringe sensor unit to do this calibration. This solution and the best method to achieve it is being investigated. It will allow us to re-calibrate the piston introduced by the influence function in case of aging of the mirror or since the DM might be sensitive to the environmental conditions which are different between Garching and Paranal

7.2.2 The Hysteresis effect of the piezoelectric bimorph mirror.

Our 35 elements bimorph mirror has an 11% hysteresis effect. For the MACAO 60-elements mirror 7% has been specified (RD 7). It acts on the DM shape in the same manner as the control signal because both are linked to the DM surface shape by the Poisson equation (Kokorowski 1978) which is linear. Thus when a potential signal corresponding to some Zernike mode is applied, the DM shape will contain not only the applied mode, but also some other modes probably including piston. This is because of the non-linearity of the mirror response due to hysteresis. In close loop the effect is reduced since the additional signal is subtracted at the next iteration, except for the piston which is not sensed. Therefore the contribution of this term on piston can be significant. Our first analytical calculations of hysteresis lead to a maximum r.m.s of piston (wavefront) of 1nm over 48ms, and of 8nm over 290ms.

7.2.3 The Resonance oscillations of the DM.

It is not excluded, however, that the control signals applied to DM might contain non-zero power at some of the DM resonant frequencies, and hence may excite additional oscillations. Introducing the proper dynamic of the DM into the simulation, we computed that the contributions of resonant frequencies should remains negligible by several order of magnitudes.

To really test the presence of resonant oscillations, it will be necessary to monitor the position of DM (some part of it) with high temporal resolution (<0.5 ms) in real time with working AO. Resonance will manifest itself in the signal power spectrum as a sharp line. If resonance turns out to be a problem, temporal filtering of control signals will be necessary. Such filtering would reduce the drive signal power at resonant frequencies to acceptable level. We hope that this can be done without adverse effect on the servo bandwidth and stability.

7.2.4 M8 Tip-Tilt stage.

By design the rotation axis of the tip-tilt stage will be located on the DM surface. Because of misalignment of the TTM rotation point with the mirror centre, it can introduce a small piston when the mirror correct for tip and tilt. The mechanical stroke of the rotation is $\alpha=\pm$ 58mrad. It can be easily demonstrated that the piston term (wavefront) introduced is proportional to a longitudinal misalignment by a factor of α^2 and to a lateral misalignment by a factor of α. Taking into consideration a 20s exposure of a **mv=20 [really?]** star for median Paranal seeing conditions, we found a piston WFE of 5.6nm rms (taking +/-0.2mm misalignment error).

7.2.5 Conclusions

The following table summarises our results:

Piston Error Source	Piston r.m.s (48ms)	Piston r.m.s (290ms)	Piston PTV (10 min)
Imperfect Removal	18 nm	26 nm	76 nm
Hysteresis	1nm	8nm	<700nm
Tip/Tilt misalignment	5.6nm	<5.6nm	<34nm
Mirror resonance	<<1nm	<<1nm	<<1nm
Total Piston Error	**19nm**	**28 nm**	**<810 nm**
VLTI Specification	**25 nm**	**125nm**	**2000nm**

Table 7-1: Piston Error Budget

In this error budget we assume no vibration of the M9 tower or M9 to M12 mirrors. We are very confident that the membrane vibration will not introduce any vibration of these components. If this turns out to be a problem, measures will be taken to shield properly MACAO and its electronic with the mechanical structure.

An agreement has been finalised with ONERA for a piston measurement set up: they will provide a set up to measure the piston introduced in closed loop operations with the required accuracy and sampling frequency. This will enable us to verify the piston specifications. We also progressed in the understanding of the piston effect using a FEM simulation of the deformable mirror that resulted in an improved piston removal algorithm, which will be double-checked by the same third party.
A back up solution would be to use the piston sensor mounted on the DM in closed loop. This sensor measure the absolute displacement of the centre of the mirror with an accuracy better than 1nm on a large bandwidth.

7.3 MACAO FOV and membrane radius of curvature

The MACAO FOV with a *flat membrane* is given by the lenslets diameter of the 2nd lenslet array (LA). The diameter of 0.7 mm translates into 4.4” FOV.
In the case of an *vibrating membrane*, field position translates into beam shift on the 1st LA. A larger membrane stroke, i.e. a smaller radius of curvature (ROC), creates a larger shift and therefore a smaller FOV depending on the size of the 1st LA. The net effect of an extended source would be to superimpose various field positions, creating a blurred enlarged beam. As shown in the figure (MACAO FOV), the MACAO membrane mirror driven at 50 cm ROC limits the FOV to only 0.8”.

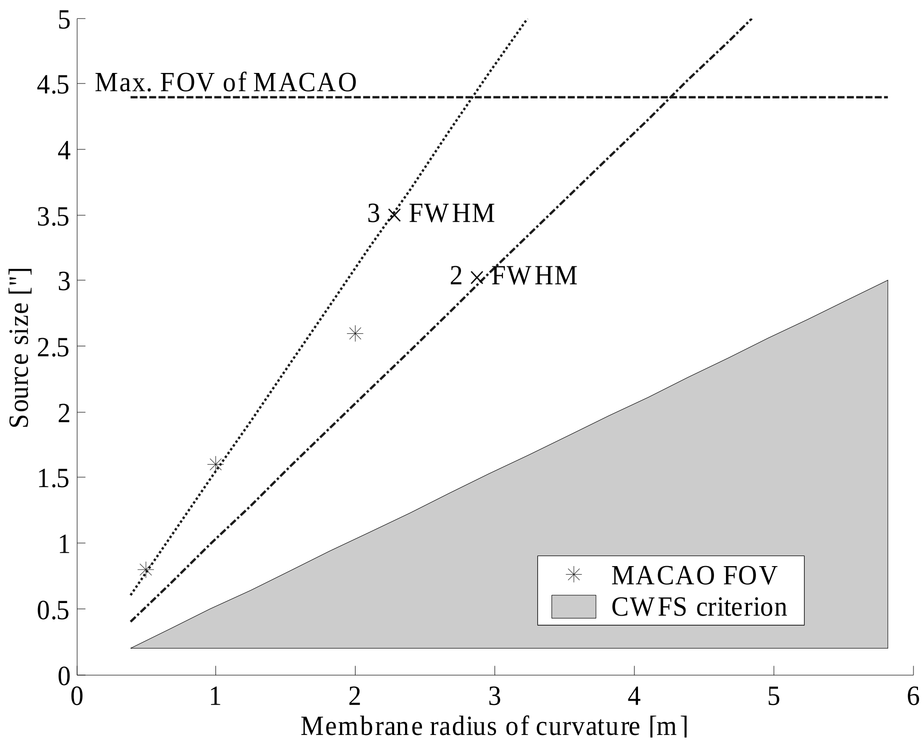

Figure 7-2: The grey area describes the range in which the MACAO CWFS will be used according to the criterion described in this section. For example, for a source size of 1” FWHM, the system will never be used with a membrane RoC less than 2m. Also shown is the MA

This sounds like a small number, but there is another criterion to consider. For successful operation of a curvature wavefront sensors (CWFS), it exists a minimum ROC depending on the source size given by either source extension or seeing. Precisely, the following relation has to be fulfilled:

$$r > \Theta \cdot \frac{f^2}{d},$$

with r denoting the ROC, Θ the source size, f the telescopes focal length, and d the subaperture size. Physically, this relation describes a trade-off between the scale of pupil blur created by the source size and the scale on which the wavefront is sampled given by the SA diameter at the position (extra-focal distance) of the mircolens array.

The possible ROCs as depending on source size as given by the criterion (VLT Coude: $f \approx 400$ m, $d \approx 0.8$ m) are drawn by the grey shaded area to the lower right of the figure. It can be seen that a ROC of 50 cm, leading to a 0.8” FOV, can only be used for source sizes of less than 0.3” which only happens in exceptionally good seeing. In this case, the FOV of the MACAO CWFS would still be three times larger than the source FWHM virtually avoiding any losses of light. For the case of a source extended by 1.5”, an ROC of about 3m has to be used giving a MACAO FOV of more than 3”. The losses outside this FOV of about 2 FWHM are well below 10%.

The conclusion is that both quantities, the source size implying a certain ROC and the resulting FOV, vary in the same way, allowing for observations under normal conditions with virtually no losses of light.

7.4 TIP/TILT RESIDUAL

We computed the tip/tilt residual that MACAO-VLTI should deliver from the same simulations used to estimate the overall system performance. To compute this residual we determine at each control cycle where the peak of the instantaneous PSF is. This procedure is limited to the resolution of the PSF as implemented in the simulation, which is 14.18 mas per pixel. A typical residual for tip and tilt is shown in Figure 7-3. Following is a summary table with the tip/tilt residuals computed with the simulation (i.e.: no error budget included). This table has been computed using the values resulting from the simulation to fit a gaussian in order to improve the resolution.

	0.65” seeing	1” seeing
Mv = 8	10.1 mas RMS (20 s)	17.1 mas RMS
Mv=10	11.1 mas RMS	17.4 mas RMS
Mv=15.5	26.3 mas RMS (20 s)	68.9 mas RMS

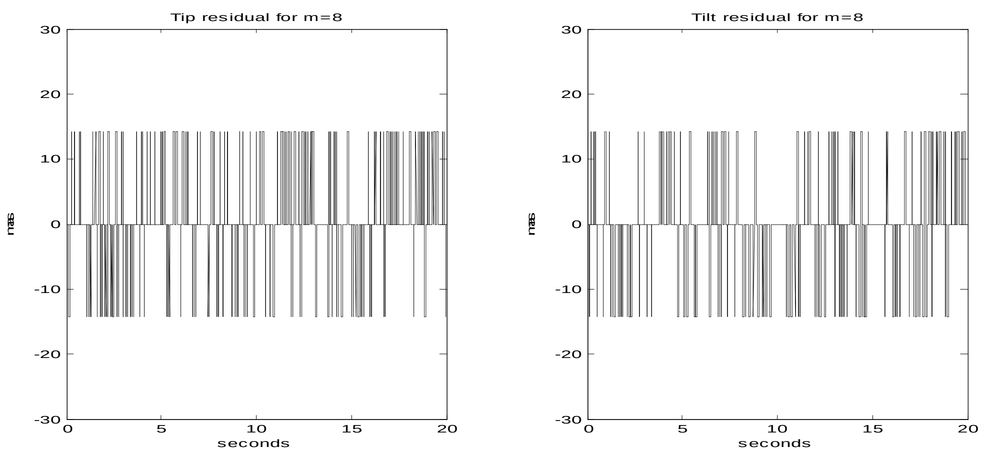

Figure 7-3: Tip/Tilt residual for a star of m=8 as measured with the simulation.

8 ERROR BUDGET

In order to compute the final performances of MACAO-VLTI, we take into account the error budget given by the numerical simulations and the estimated error budget for all the subsystems not considered in the simulations.

8.1 Reference conditions

The reference conditions for MACAO-VLTI are those listed in section 5.1.1 and 5.2.2, and we list here the most important ones:

- seeing at zenith: 0.65" and 1" (@ 0.5μm)
- outer scale of turbulence: infinite
- coherence time: 4ms
- reference source: point-like and on axis
- WFS effective wavelength: 0.7μm

8.2 Wavefront Error Budget

We will show here that the final Strehl Ratio achieved taking into account both numerical simulations WFE and other subsystems WFE matches the requirements given in AD 2.

The Strehl Ratio requirements for MACAO-VLTI at 2.2μm and the WFE budget from numerical simulations are listed in Table 8-1. All the WFE values are in nm rms.

NGS Visual magnitude	Strehl Ratio	RMS (nm)
8.0	0.50	292
14.5	0.35	359
15.5	0.25	412

Table 8-1: Wavefront error requirements for MACAO-VLTI from AD 2

The WFE, without optical errors, given by the numerical simulations at 2.2μm are listed in Table 8-2.

NGS Visual magnitude	Strehl Ratio	RMS (nm)
8.0	0.66	226
14.5	0.47	304
15.5	0.34	364

Table 8-2: Wavefront error from numerical simulations

A detailed WFE list relative to each subsystem not included in the numerical simulations that will affect the performance of the AO correction is given below. These errors are shown in Table 8-3 and the resulting total RMS is computed.

8.2.1 Error Budget Table

No	Name	WFE	Reference
1	Telescope Optics (M1 + M2 + M3)	40 nm	Internal Communication (P. Dierickx)
2	Coudé Optics (from M4 to M8)	41 nm	VLT UT Coude' Error Budget, A. Michel
3	DM High Spatial Freq. Optical Quality Best Flat	30 nm	VLT-SOW-ESO-11640-2064 3.1.1
4	DM High Spatial Freq. Optical quality roughness	3 nm	VLT-SOW-ESO-11640-2064 3.1.1
5	M9 optical quality (transmission)	35 nm	Internal Communication (B. Delabre)
6	Telecentricity optical quality (on axis)	25 nm	Internal Communication (B. Delabre)
7	Pupil superimposition error on WFS	50 nm	VLT-SPE-ESO-15600-2126 5.1.3
8	WFS box XY positioning stability at Zenith	28 nm	VLT-TRE-ESO-11640-1661 3.5
9	Pupil superimposition error on DM	31 nm	IDL simulations
10	Interaction matrix recording SNR	35 nm	VLT-TRE-NAO-11650-9040 §7
11	Tip-Tilt mirror resolution	10 nm	VLT-SPE-ESO-11640-2147 2.3
12	Atmospheric dispersion near Zenith	<1 nm	Estimation
13	Scintillation	10 nm	Estimation
	TOTAL (summed in quadrature)	**108 nm**	

Table 8-3: Wavefront error of the sub-systems not included in the numerical simulations

There are 3 categories of errors taken into account into Table 8-3 and the following discussion. According to Figure 8-1, all the wavefront errors present in the common path (1) should be cancelled by the AO system. Some errors are present at a spatial frequency that the wavefront sensor cannot detect (items 1, 2, 3 and 4).

In particular for item 1, at 500nm we have for the WFE of M1+M2+M3:

- UT1: 0.726 → 45 nm
- UT2: 0.808 → 37 nm
- UT3: 0.785 → 39 nm

Average: 40 nm
For item 2, M8 is considered to have 7nm of polishing error (VLT-SPE-ESO-15600-2064 defines 3nm).

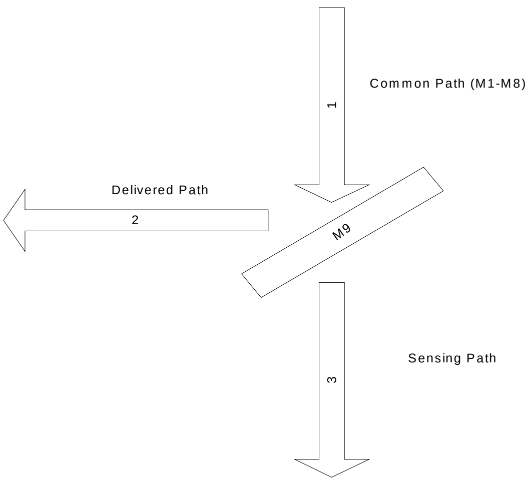

Figure 8-1: Error distribution

Others wavefront errors are present only after the dichroic, so present only in the beam going to the wavefront sensor and not in the output beam, so the AO system will correct for an additional error (items 5 and 6)

Others errors come from misalignments and mechanical errors (items 7, 8, 9, 11).
In particular, for item 7 we considered the following budget:

	Displacement	Angle	Relative to pupil	On lenslet
WFS beam rotator	10 µm	-	0.07%	10 µm
ND filter	100 µm	-	0.70%	100 µm
XY table travelling error	-	15”	0.35%	49 µm
Membrane gimbal accuracy	-	2”/axis	0.28%	40 µm
Lenslet torque	< 0.5 µm	-	negligible	Negligible
Total			0.85%	119 µm

This number was then used to simulate the pupil displacement on the WFS using our simulation tool.
Item 9 takes into account the error introduced by the DM correction when it is displaced with respect to the position at which the interaction matrix has been recorded. This has been carried out with an IDL simulation that computes the error introduced by each mode by computing the variance of the residual wavefront obtained subtracting the mode phase (fitted by the mirror) to the mode phase itself shifted laterally by a certain amount.
The overall variance error is the sum of all variances accordingly weighted by the atmospheric spectrum.
The opposite behaviour, i.e.: the positioning error of the pupil over a well-positioned M8 doesn’t cause errors and the DM will correct a displaced pupil.

8.2.2 Combined Error Budget

Finally, the WFE after M9 in transmission is computed and the final Strehl Ratio in K band (2.2µm) is given in Table 8-4.

NGS visual mag.	Simulation WFE	Other WFE	Total WFE	Strehl Ratio	Req. SR
8.0	226	**108**	**250**	**0.60**	0.50
14.5	304	**108**	**323**	**0.43**	0.35
15.5	364	**108**	**380**	**0.31**	0.25

Table 8-4: WFE@M9 for MACAO-VLTI with 0.65” seeing

In the case we consider a worse seeing condition of 1”, the overall performances decrease as shown in Table 8-5.

NGS visual mag.	Simulation WFE	Other WFE	Total WFE	Strehl Ratio	Req. SR
8.0	317	**108**	**335**	**0.40**	0.30
14.5	418	**108**	**432**	**~0.22**[3]	N/A
15.5	491	**108**	**503**	**~0.13**	N/A

Table 8-5: WFE@M9 for MACAO-VLTI with 1” seeing

[3] The formula used to compute the Strehl ratio from the WFE is not accurate at this range, but doesn’t need to be compared with a requirement.

Simulations have been performed without taking into account the light losses due to the internal wavefront sensor reflections, the lenslet array itself and the fiber optics coupling. As shown in section 5.1.3.2 these sources cause a loss of 28% of light, globally and on average. This corresponds, approximately, of a shift in magnitude of 0.36, which has been applied to the curves in Figure 8-2.

And additional error will be present after M9 (path 2 in Figure 8-1) due to its own aberrations in reflection:

No	Name	WFE	Reference
14	M9 optical quality (reflection)[4]	35 nm	Internal Communication (B. Delabre)
15	M9 tilt stability (reflection)	28 nm	Requirement. In case of 2mas
16	M9 induced aberrations (reflection)[5]	50 nm	Internal Communication (B. Delabre)
	TOTAL (summed in quadrature)	67nm	

8.2.3 Delivered WFE

This result in the final WFE and the final Strehl Ratio in K band (2.2µm), given in Table 8-6.

NGS visual mag.	AO WFE	Other WFE	Total WFE	Strehl Ratio	Req. SR
8.0	**249**	**67**	**258**	**0.58**	0.50
14.5	**322**	**67**	**329**	**0.41**	0.35
15.5	**379**	**67**	**385**	**0.30**	0.25

Table 8-6: Total WFE for MACAO-VLTI with 0.65” seeing

In the case we consider a worse seeing condition of 1”, the overall performances decrease as shown in Table 8-7.

NGS visual mag.	AO WFE	Other WFE	Total WFE	Strehl Ratio	Req. SR
8.0	**334**	**67**	**346**	**0.38**	0.30
14.5	**431**	**67**	**439**	**~0.21**	N/A
15.5	**502**	**67**	**508**	**~0.12**	N/A

Table 8-7: Total WFE for MACAO-VLTI with 1” seeing

[4] Refers to high spatial frequency errors due to optical manufacturing and multi-layer coatings.
[5] Refers to possible deformations and flexures producing low spatial frequency aberrations (i.e.: astigmatism).

8.3 RESULTS

In conclusion, it is our belief that we will meet, or exceed, all the requirements set out in AD 2, which in turn meet all the top level requirements of VLTI AO (AD 1). Figure 8-2 shows the final expected performance of the system, in which the error budget is taken into account, along with the required Strehl Ratios.

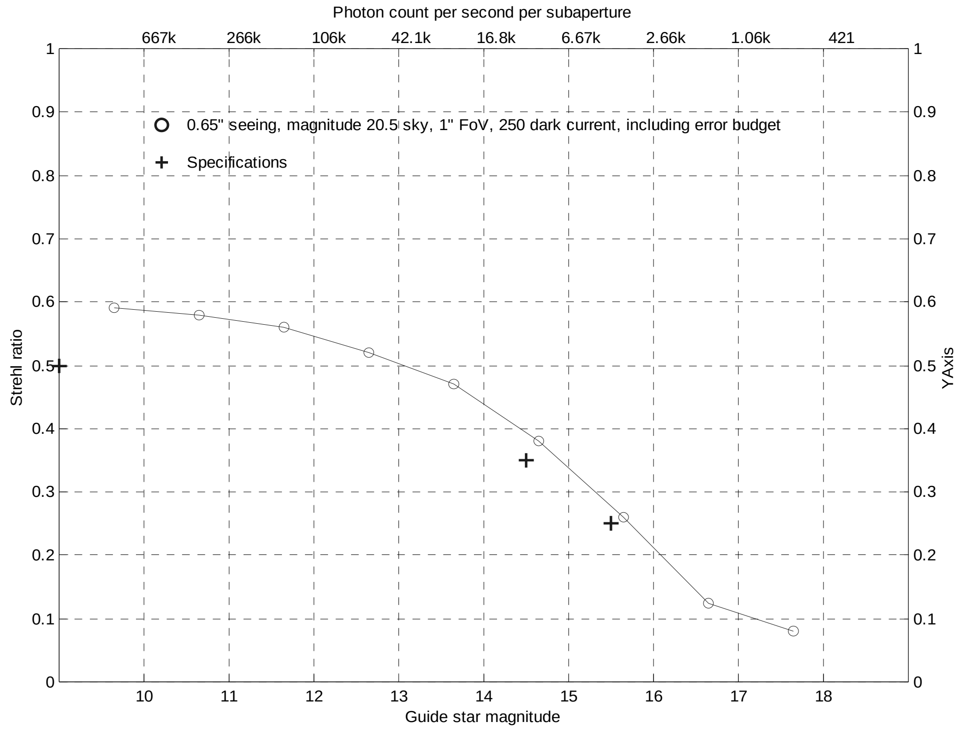

Figure 8-2: Performance curves with the error budget taken into account